JM3 Journal of Micro/Nanopatterning, Materials, and Metrology

RESEARCH PAPER

Characterization of latent image of electron beam resist via critical-dimension resonant soft X-ray scattering

Qi Zhang,[a,b,c,†] Kas Andrle,[a,†] Weilun Chao,[a,b] Zhengxing Peng,[a] Warren Holcomb,[a,b] Ryan Miyakawa,[a,b] Dinesh Kumar,[d] Alexander Hexemer,[c] Patrick Naulleau,[a,b] Bruno La Fontaine,[a,b] Ricardo Ruiz,[e] and Cheng Wang[c,*]

[a]Lawrence Berkeley National Laboratory, Materials Science Division, Berkeley, California, United States
[b]Lawrence Berkeley National Laboratory, Center for X-Ray Optics, Berkeley, California, United States
[c]Lawrence Berkeley National Laboratory, Advanced Light Source, Berkeley, California, United States
[d]Center for Advanced Mathematics for Energy Research Applications, Lawrence Berkeley National Laboratory, Berkeley, California, United States
[e]Lawrence Berkeley National Laboratory, The Molecular Foundry, Berkeley, California, United States

ABSTRACT. Metrology plays a crucial role in semiconductor manufacturing by providing accurate and precise measurement and characterization of critical parameters. With the development of high-resolution extreme ultraviolet lithography (EUVL) processes, critical dimensions are shrinking to sub-10 nm. Resist materials encounter the challenge of providing heightened sensitivity and a handle on exacerbating stochastic variations. A comprehensive understanding of the chemical profile of the latent image is pivotal for mitigating stochastic effects and optimizing pattern quality. However, the subtle differences in chemistry between the exposed and unexposed regions of the resists make it extremely challenging to characterize the latent images with sub-nanometer precision. Here, we develop the metrology with critical-dimension resonant soft X-ray scattering (CD-RSoXS) to probe the chemical profiles of latent images stored in resist after exposure. The combination of absorption spectroscopy and enhanced scattering contrast makes it possible to characterize the subtle structural and chemical variations in the latent image. Moreover, the results of the measurements are compared with the simulations with a finite element method–based Maxwell solver to extract a detailed profile of the latent and developed images. We demonstrate that the CD-RSoXS technique can provide valuable insights into the high spatial resolution and local chemical sensitivity simultaneously, which is crucial to understanding the resolution limits and stochastic effects in EUVL processes.

Keywords: latent image; chemical information; resonant soft X-ray; scattering; finite element method

Paper 24047G received Jul. 12, 2024; revised Sep. 22, 2024; accepted Sep. 25, 2024; published Oct. 18, 2024.

1 Introduction

In the realm of advanced semiconductor manufacturing, extreme ultraviolet lithography (EUVL) has emerged as a pivotal technology enabling the continued miniaturization of electronic

*Address all correspondence to Cheng Wang, cwang2@lbl.gov

†These authors contributed equally to this work.

devices.[1] However, at the forefront of EUVL challenges are the stochastic effects, which can significantly impact pattern fidelity and critical dimension control.[2–4] Stochastic effects manifest as random variations in the formation of features during the exposure of resist materials to extreme ultraviolet (EUV) light. As EUV progresses toward higher resolutions with next-generation high numerical aperture (NA) and hyper NA, resist materials encounter the formidable challenge of providing heightened sensitivity and a handle on exacerbating stochastic variations.[5–7] Therefore, comprehensive understanding of the stochastic nature of structural and chemical phenomena that occur during the formation of high-precision patterns in photoresists is highly desirable.

Currently, there are various powerful means to probe and quantify stochastic effects in the developed patterns. Critical dimension scanning electron microscopy stands as a cornerstone technique in semiconductor metrology, providing invaluable insights into the critical dimensions of nanoscale features.[8–10] CD atomic force microscopy (AFM) can also provide topographical information by scanning a sharp tip over the surface of a sample.[11,12] It is particularly useful for measuring surface roughness. In addition, critical-dimension small-angle X-ray scattering (CD-SAXS) emerges as a formidable technique for elucidating the nanoscale structure of thin films and patterned features.[13–15] CD-SAXS, by analyzing the scattering of X-rays at small angles, can provide information about feature dimensions, shape, and spatial correlations, making it valuable for CD metrology in advanced lithography. Here, a notable constraint in the ability to model, measure, and refine photoresist materials lies in the fact that the assessment of patterning performance currently occurs after the development process. More importantly, only the structural information can be extracted from these abovementioned CD metrology techniques. The latent image, a transient state formed during the exposure of a resist material to EUV light, can provide beneficial information about the final pattern that will eventually be transferred onto the substrate. Understanding and accurately characterizing the chemical and structural information in the latent image is critical for optimizing process parameters, ensuring pattern fidelity, and ultimately informing the co-design of new EUV resists.

In this paper, we introduce critical-dimension resonant soft X-ray scattering (CD-RSoXS) to probe the scattering behavior of latent images at specific resonant photon energies. CD-RSoXS leverages tunable soft X-rays to get the resonant excitation and dramatically enhance the scattering cross-sections from heterogeneous materials when the X-ray photon energy is adjusted to match a given element X-ray absorption edges.[16–18] The combination of absorption spectroscopy and scattering enhances the scattering contrast due to subtle structural and chemical variations in the latent images.[19] This technique offers a unique advantage over traditional metrology methods, as it can provide valuable insights into the high spatial resolution and local chemical sensitivity simultaneously.

2 Experimental Section

2.1 Sample Fabrication

To systematically study the latent images with CD-RSoXS, a commercial Zeon Electron beam Positive-tone resist (ZEP) was employed as the initial testing sample in this paper. E-beam can serve as a reliable proxy for EUV due to their similar resist interaction mechanisms. Both techniques generate secondary electrons that initiate chemical reactions in the resist, making the E-beam a valuable tool for studying resist performance. In addition, E-beam lithography offers a greater flexibility in achieving uniform features, facilitating quantitative analysis and the construction of initial models. Samples were fabricated with various line pitches, ranging from 100 to 40 nm. The fabrication began with dehydrating the substrate, featuring freestanding 100-nm-thick silicon nitride (SiN_x) membrane windows, on a hotplate at 110°C for 90 s. Following cooling, hexamethyldisilazane was spin-coated onto the substrate, which was then baked at 110°C for 2 min. Subsequently, the resist was spin-coated onto a standard SiN_x window on Si wafers to create a film ~40 nm thick. A post-application bake was then conducted for 5 min at 170°C. Line grating patterns, with a line width of 16 nm narrower than the designed half pitch values (50, 40, 30, 20 nm), were exposed on membrane windows using a 100-keV Raith EBPG5200 tool at Molecular Foundry, Lawrence Berkeley National Laboratory (LBNL). The exposed area covered the entire SiN_x window, measuring 0.5 mm × 0.5 mm, as illustrated in

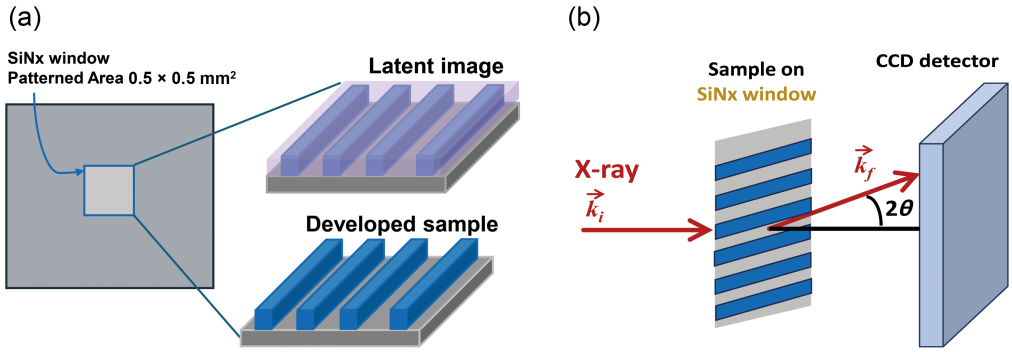

Fig. 1 (a) Illustration of the latent image and developed sample on SiN_x windows. (b) Illustration of CD-RSoXS with the beam path in transmission geometry.

Fig. 1(a). Subsequently, latent images were acquired post-exposure, whereas the developed samples underwent processing through a dissolution procedure. The substrate was developed in hexyl acetate for 30 s, dipped in pentane for 5 s, and then blow-dried with nitrogen. Different line pitches were exposed with varying dosages. Specifically, 100 and 80 nm line gratings were exposed at 1.5 mC/cm^2, whereas dosages of 1.7 and 4.5 mC/cm^2 were used for the 60- and 40-nm pitches, respectively.

2.2 CD-RSoXS Measurement

CD-RSoXS experiments were performed at beamline 11.0.1.2 of the Advanced Light Source (ALS), LBNL.[20] The X-ray beam has an elliptical shape with approximate diameters of 400 and 200 μm. The dose we used for CD-RSoXS measurement is around 0.35 $mJ/cm^2 \cdot s$. The charge-coupled device (CCD) camera was positioned at varying distances, depending upon the line pitch of the samples. Measurements were conducted at the carbon K-edge, specifically within the energy range of 280 to 300 eV. The line grating samples were manually aligned, ensuring the diffraction peaks to be captured by the CCD, as illustrated in Fig. 1(b). In our experiments, we used the normal incident angle. The exposure time was optimized to balance signal-to-noise ratio, avoid detector saturation, and minimize radiation dose to prevent beam damage. The exposure time ranges from 1 ms up to 2 s. It is crucial to consider the X-ray probe beam damage, particularly for latent images, during prolonged exposure times. The minimum exposure time (1 ms) was achieved using a piezo shutter. Radiation dose can be further adjusted by tuning the incident beam intensity.

2.3 Atomic Force Microscopy

The topographic imaging of the fabricated samples was captured using AFM. AFM images were acquired using the Bruker Dimension Icon3 in ScanAsyst mode at the Molecular Foundry, LBNL. The ScanAsyst probe was paired with a sharp tip ranging from 2 to 12 nm in radius. The thickness and cross-section profile were extracted from the AFM images.

3 Results and Discussion

3.1 Near-Edge X-ray Absorption Fine Structure

To investigate the chemical alterations occurring in a resist during the exposure process, we conducted near-edge X-ray absorption fine structure (NEXAFS) spectroscopy separately on the uniform pristine and exposed resist films at ALS beamline 11.0.1.2. This established technique leverages the photoexcitation of electrons from a core level to unoccupied molecular orbitals, providing detailed insights into the precise chemical surroundings of a particular element. NEXAFS at the carbon edge is particularly suitable to analyze the chemical environment of the resists.[21,22] As shown in Fig. 2(a), NEXAFS reveals two primary peaks changed after exposure. The peak at 285.2 eV may belong to the π^* C=C resonance of the carbon–carbon double bonds.[23] The sharp peak at 288.6 eV may be attributed to C=O double bonds in the methacrylate group.[23] These two resonant energies will be used for CD-RSoXS measurement.

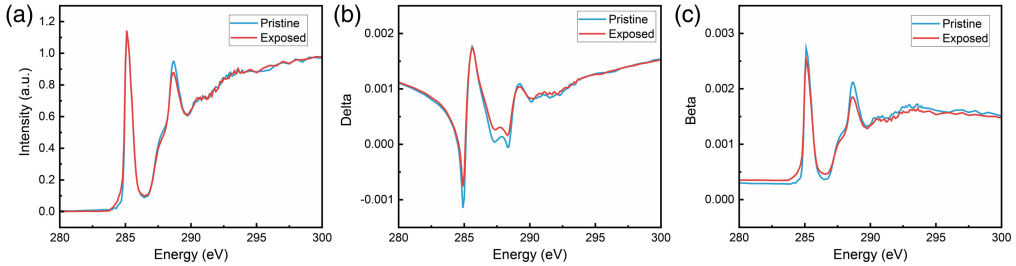

Fig. 2 (a) NEXAFS spectra for unexposed and exposed resists. Optical constants delta (b) and beta (c) as a function of energy for unexposed and exposed resists.

Furthermore, optical constant, delta (δ) and beta (β) in the complex index of refraction $n(E) = 1 - \delta(E) + i\beta(E)$ can be determined from NEXAFS spectra, which was measured at ALS beamline 11.0.1.2 with total electron yield (TEY) mode. The absorption part of the index of refraction β can be indirectly extracted by TEY measurements[24] and then scaled to the Henke atomic scattering factor database.[25] The dispersion part of the index of refraction δ can be determined with the Kramers–Kronig relations.[26,27] The energy dependence of delta and beta are shown in Figs. 2(b) and 2(c), respectively.

3.2 CD-RSoXS Results

CD-RSoXS measurements were performed at the ALS beamline 11.0.1.2 using incident energies of 280, 285.2, and 288.6 eV. The incident angle was constant normal incidence. Scattering intensity was captured on a CCD detector featuring a pixel size of 27 μm and a sample-to-detector distance of 70 mm. The exposure times are 2 s for the latent image and 1 ms for the developed sample, respectively.

The CD-RSoXS scattering patterns of latent image and developed samples with different line pitches are illustrated in Figs. 3(a) and 3(b), respectively. The spacing between adjacent diffraction orders corresponds to the line pitch number. It is apparent that varying intensities are observed among different diffraction orders in latent images. Specifically, in the developed sample, the intensity of the second order is lower than that of the third order. However, in the latent image [as depicted in Fig. 3(a)], the intensity of the second order surpasses that of the third order. The one-dimensional (1D) q-space lineouts of the scattering intensity at 280 eV clearly delineate the distinction between latent image and developed sample with varying line pitches [Fig. 3(c)].

To unveil the origin of such differences in scattering intensity, we conducted AFM to examine the structural differences between the latent image and the developed sample. AFM images reveal distinct structural features of the latent image [Fig. 4(a)] and the developed sample [Fig. 4(b)]. Notably, a reduction in thickness within the exposed area is observed in the latent image. Upon closer examination of the cross-sectional profile [Fig. 4(c)], it becomes apparent

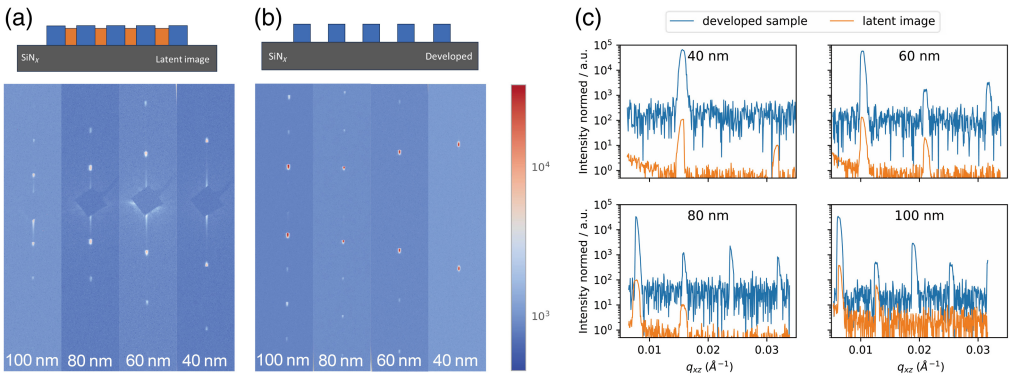

Fig. 3 CD-RSoXS scattering patterns of (a) latent image and (b) developed sample in transmission geometry. (c) 1D plots of the scattering intensity at 280 eV of latent image and developed sample with varying line pitches (40, 60, 80, and 100 nm).

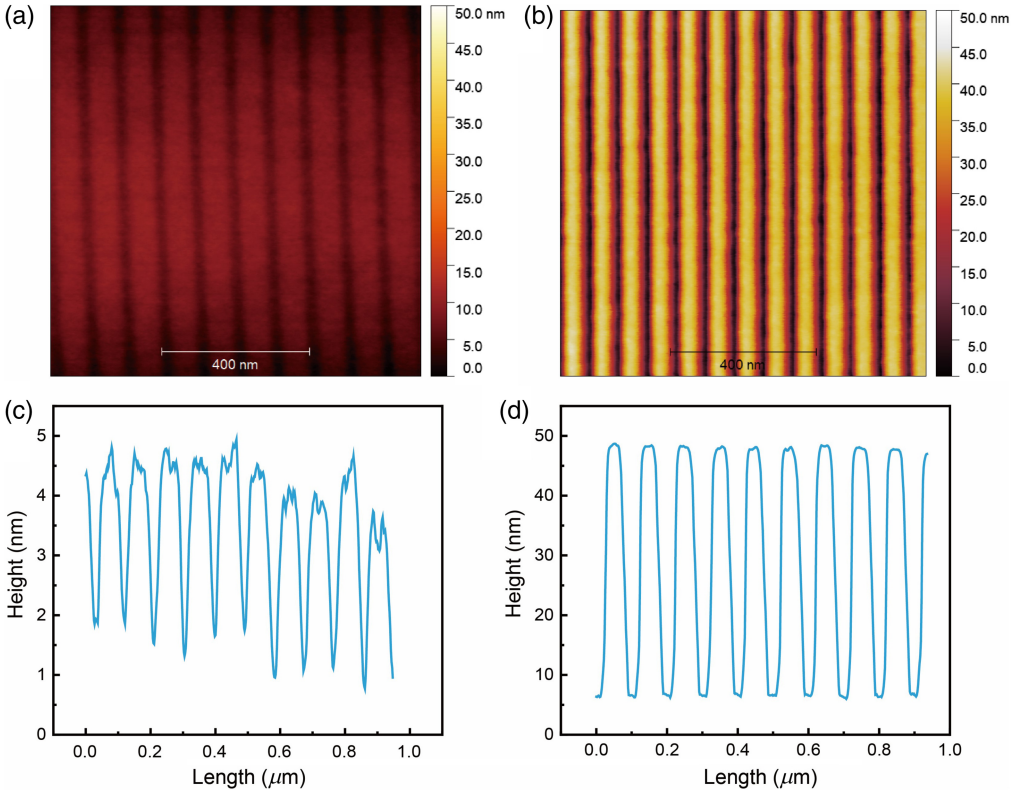

Fig. 4 AFM images of (a) latent image and (b) developed sample with 100-nm pitch. Cross-section profiles of (c) latent image and (d) developed sample.

that the line width with reduced thickness measures less than half the pitch. In contrast, in the developed sample, the width of the lines nearly matches the width of the spaces (or trenches) between them, as illustrated in Fig. 4(d). Such measured topography of the developed sample approaches the shape of a square wave, which explains why the even-order diffraction peaks are significantly smaller than the odd-order peaks in the corresponding scattering patterns of the developed samples.

3.3 Finite Element Method Maxwell Solver

The AFM and CD-RSoXS measurements of the gratings reveal a transformation in shape from latent image to developed gratings. This combination has been demonstrated in the characterization of directed self-assembly polymers using hard X-ray scattering.[28] It is noted that the AFM tip size ($2 \sim 12$ nm) is in the same order of magnitude as the grating, making it difficult to get the exact shape of the grating. As a result, AFM measurements primarily allow for the retrieval of the grating's height. In the latent sample, a chemical distinction exists between the exposed and unexposed regions. However, AFM is limited to surface analysis and cannot capture this chemical difference. For a deeper understanding of the cross-sections in both latent and developed samples, as well as their variations, we numerically solve Maxwell's equations using finite element method (FEM) to simulate the CD-RSoXS results. This simulation is capable of calculating the scattered intensity for complex shape.[29] To conduct the Maxwell solver simulation accurately, knowledge of the optical constants of the materials involved is essential. In the calculations presented here, the optical constants of the photoresist were derived from NEXAFS measurements (Fig. 2). Previous studies[30] have demonstrated that near an absorption edge, the optical constants deviate from database values when the corresponding element is present in the material.

Figures 5(a) and 5(c) present the reconstructed cross-sections of the latent and developed gratings, respectively. The blue section represents the SiN_x window, the grey portion indicates the unexposed area, and the green segment denotes the exposed resist. The triangulation represents the FEM mesh we used in this calculation. In our calculations, we employ periodic boundary

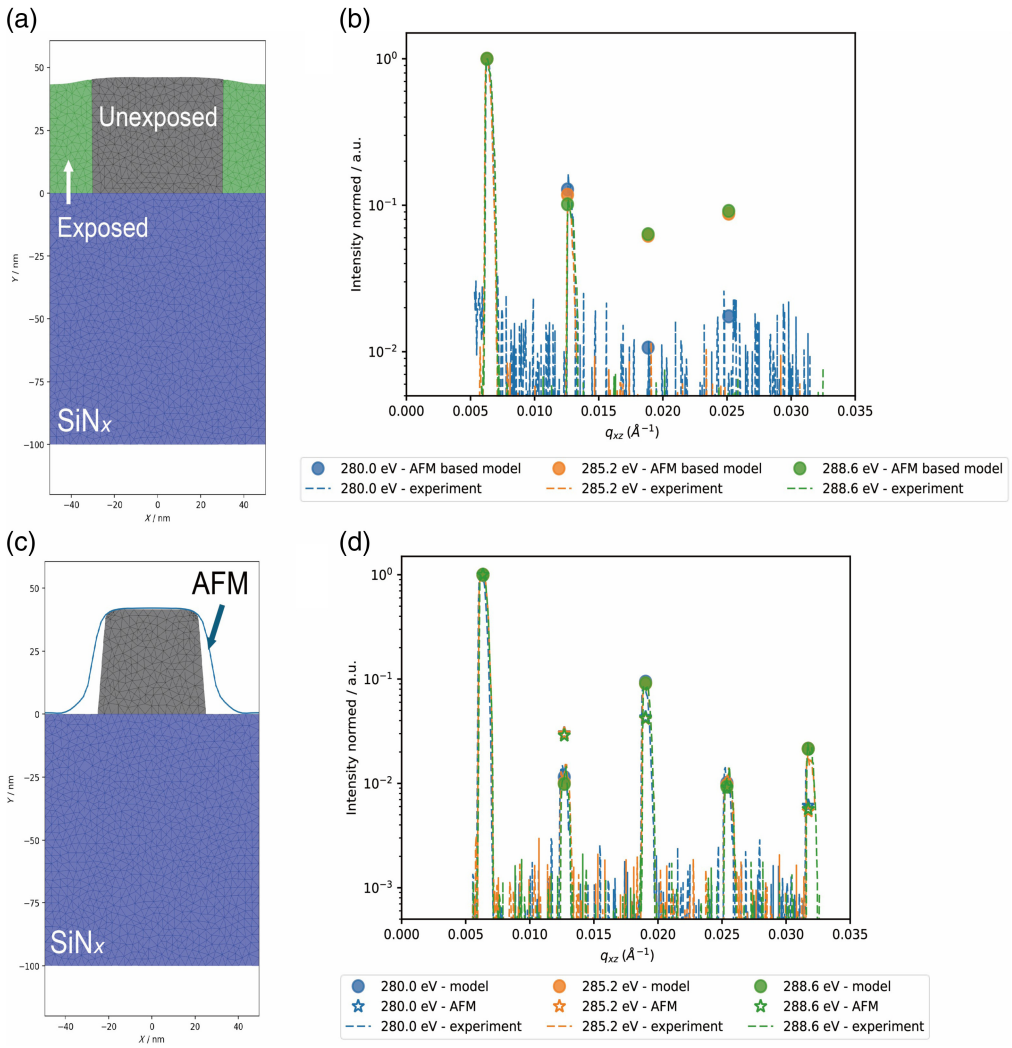

Fig. 5 Cross-section of the grating used for the FEM Maxwell solver calculation for latent (a) and developed (c) grating with the corresponding calculated scattering intensities (b) and (d) for different incident energies compared with the experimental values.

Table 1 Grating parameters extracted from simulation.

	Pitch (nm)	CD (nm)	Height (nm)
Latent image	100	50	39.3 (exposed); 41.8 (pristine)
Developed sample	100	44.4	41.8

conditions. On the right side, a comparison is made between the simulated and the measured scattering intensities [Figs. 5(b) and 5(d)]. The grating parameters of latent image and developed sample extracted from simulation are summarized in Table 1.

The initial shape of the latent grating used in the simulations was derived from the AFM measurements [Fig. 5(a)]. The height of the resist, measured at 41.8 nm, was obtained from the AFM analysis of the developed sample. A width of 60 nm was selected for the unexposed part (grey) to best represent the scattering data in first and second orders. It is worth noting that the calculated values for the third and fourth orders are presented, despite these orders not being observed in the experimental measurements of the latent image [Fig. 5(b)]. The calculation intensity was normalized to the first order, but the actual intensity of 280 eV was much lower for those of 285.2 and 288 eV due to the reduced incident beam intensity (potentially due to carbon

contamination). According to the calculations, at an incident energy of 280 eV, the third and fourth orders approach the detection limit in magnitude. This energy falls below the absorption edge, where no distinction exists among the optical constants of the exposed and unexposed resist. Furthermore, the calculated intensities of the third and fourth orders at resonant energies are slightly lower than that of the second order. Therefore, the detection limit is unlikely to be the reason, pointing to a potential model issue. We will delve into this issue in the next chapter.

For the developed sample, the high scattering intensity and contrast enable us to observe orders from the first to the fifth. We use the shape derived from the AFM measurements as an initial approximation for calculating the scattering intensities [depicted as stars in Fig. 5(d)]. Although they exhibit a similar trend to the measured values, discrepancies arise, particularly for the second and third orders. AFM struggles to capture the exact profile due to the tip's shape being comparable in magnitude to the critical dimension of the grating, complicating the determination of the grating's sidewall angle. To obtain a more detailed shape, Bayesian optimization[31] is employed to reconstruct the sidewall angle and width. The results are depicted in Fig. 5(d) (points) and align well with the measured intensities. In Fig. 5(c), the reconstructed shape is juxtaposed with the AFM-derived shape. Notably, the reconstructed shape appears smaller and has a steeper sidewall angle compared with the AFM measurement. From the reconstruction results, it is evident that the unexposed portion of the developed grating cross-section is smaller than that of the latent image, suggesting that some of the materials at the exposed gradient dissolved during the development process. These findings align with the AFM measurements and the presence of the unsuppressed second order in the CD-RSoXS measurements of the latent images.

Last, we proceed to the reconstruction of the developed sample with pitches of 60 and 80 nm (Fig. 6). For gratings of this size, obtaining shape information from AFM measurements is more challenging. The height of the gratings was fixed to the height obtained from the AFM measurement of the 100-nm pitch sample. As shown in Fig. 6, there is a good agreement between the measurements and the reconstructed diffraction order. The corresponding shapes are displayed as insets in Fig. 6. The reconstructed sidewall angle is closer to 90 deg compared with

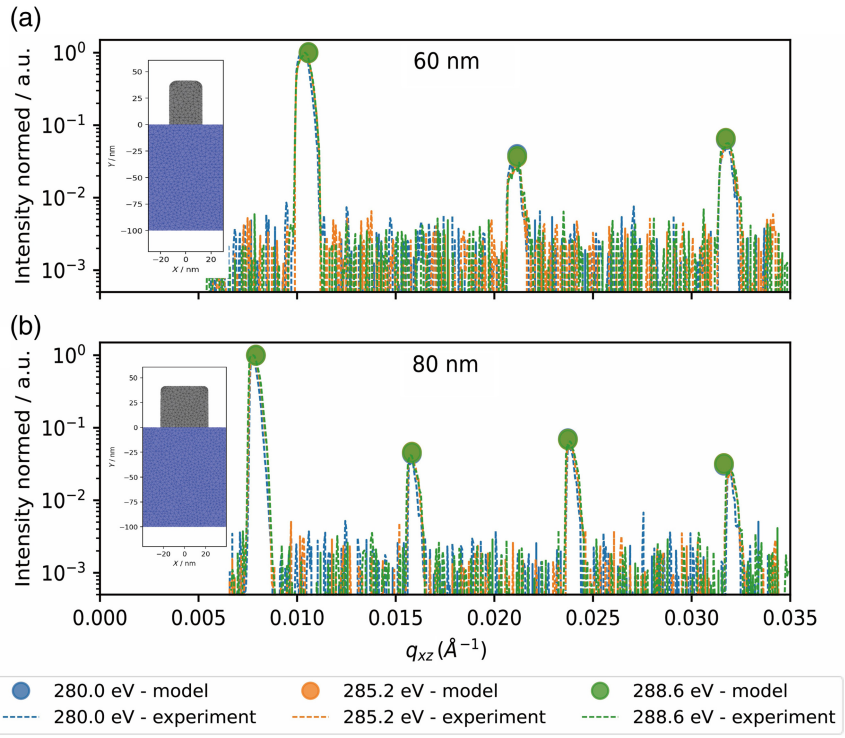

Fig. 6 Cross-section of the grating used for the FEM Maxwell solver calculation for pitch 60 nm (developed) (a) and pitch 80 nm (developed) grating with the corresponding calculated scattering intensities for different incident energies compared with the experimental values.

the 100-nm pitch sample. These differences may be clearer in the reconstruction of the latent image, which requires further study. Due to the limited number of available diffraction orders and no variation in the angle of incidence (normal incidence for all measurements), the number of model parameters is comparable to the number of available measurement points. This situation may result in overfitting and a model with high uncertainties due to the low number of degrees of freedom.

4 Discussion and Outlook

We performed CD-RSoXS measurements to investigate the scattering behavior of latent images at specific soft X-ray energies. The CD-RSoXS unveils distinct scattering patterns for both latent and developed samples with very fast data acquisition, when compared with traditional microscopy modalities. By integrating CD-AFM measurements with FEM Maxwell solver calculations, we obtained the structural and chemical attributes of the latent image within the photoresist. This enhances our understanding of the photoresist's behavior during exposure.

These findings mark the first demonstration of latent image reconstruction by combining CD-AFM with a single CD-RSoXS pattern at a normal incident angle. This approach has the potential to fundamentally revolutionize high-throughput measurements and minimize beam damage to resist materials. However, some challenges remain. Currently, we use the intensity of the first order to normalize the experimental data for simulation. In this case, the latent image does not show enough orders for an ideal reconstruction. As previously mentioned, the calculated intensities for the third and fourth orders at resonant energies are marginally lower than those for the second order, a discrepancy not observed in the experimental data. Several factors warrant consideration for continued research in the field. First, the inclusion of roughness effects in the modeling will be crucial for understanding the origins of stochastic effects.[32] In addition, gradients may exist between the exposed and unexposed areas, offering valuable insights into the details of photon/electron-driven reactions at the interface.[32] As we develop the technique further to enhance the accuracy of the reconstruction of the two-dimensional cross-sections and include uncertainties,[33] in the experiment, the number of data points will be increased by measuring the scattering over a larger range of angles and/or incident energies. This will decrease the uncertainties of the different model parameters and enable the possibility to obtain detailed information about the shape of the structure. Overall, advancing CD metrology through RSoXS is promising for understanding the origins of stochastic effects and informing the co-design of new resist materials.

Disclosures

The authors declare no competing interests.

Code and Data Availability

All the data supporting the findings of this study are available from the corresponding author upon request.

Acknowledgments

Research is supported as part of the CHiPPS, an Energy Frontier Research Center funded by the U.S. Department of Energy (DOE), Office of Science, Basic Energy Sciences. This research used resources from the Advanced Light Source, which is a DOE Office of Science User Facility (Grant No. DE-AC02-05CH11231). Work at the Molecular Foundry was supported by the Office of Science, Office of Basic Energy Sciences, of the U.S. Department of Energy (Grant No. DE-AC02-05CH11231). We thank Andrew Neureuther for the discussion on simulation and modeling. The FEM calculations were conducted on the NERSC supercomputer.

References

1. E. R. Hosler, "Bringing manufacturing to quantum computing: the path to a million qubits," *Proc. SPIE* **11854**, 1185402 (2021).
2. P. Naulleau, "Chapter 5—EUV lithography patterning challenges," *Front. Nanosci.* **11**, 177–192 (2016).

3. H. J. Levinson and T. A. Brunner, "Current challenges and opportunities for EUV lithography," *Proc. SPIE* **10809**, 1080903 (2018).
4. A. Grenville et al., "Delivering metal oxide photoresists for EUV: overcoming challenges to scaling," *Proc. SPIE* **11326**, 1132610 (2020).
5. S. Bhattarai et al., "Simulation analysis of LER and dose tradeoffs for EUV resists with photo-decomposable quenchers," *Proc. SPIE* **8679**, 867925 (2013).
6. R. Gronheid et al., "Resolution-linewidth roughness-sensitivity performance tradeoffs for an extreme ultraviolet polymer bound photo-acid generator resist," *Proc. SPIE* **10**, 013017 (2011).
7. T. Manouras et al., "Ultra-sensitive EUV resists based on acid-catalyzed polymer backbone breaking," *Proc. SPIE* **10583**, 105831R (2018).
8. B. Bunday et al., "Determination of optimal parameters for CD-SEM measurement of line-edge roughness," *Proc. SPIE* **5375**, 515–533 (2004).
9. C. G. Frase et al., "CD characterization of nanostructures in SEM metrology," *Meas. Sci. Technol.* **18**(2), 510 (2007).
10. C. A. Mack et al., "Diagnosing and removing CD-SEM metrology artifacts," *Proc. SPIE* **11611**, 116111B (2021).
11. P. Nealey et al., "Characterization of the shape and line-edge roughness of polymer gratings with grazing incidence small-angle X-ray scattering and atomic force microscopy," *J. Appl. Crystallogr.* **49**(3), 823–834 (2016).
12. G. Dai et al., *Recent Progress and Challenges in AFM-Based True-3D Micro and Nanometrology*, TU Ilmenau (2023).
13. J. Ronald, et al, "Characterization of line edge roughness using CD-SAXS," *Proc. SPIE* **6152**, 61520N (2006).
14. Y. Ito et al., "Characterization of cross-sectional profile of resist L/S and hole pattern using CD-SAXS," *Proc. SPIE* **9778**, 97780L (2016).
15. M. Fan et al., "High resolution profiles of 3D NAND pillars using X-ray scattering metrology," *Proc. SPIE* **11611**, 116110S (2021).
16. W. Zhong et al., "Decoupling complex multi-length-scale morphology in non-fullerene photovoltaics with nitrogen K-edge resonant soft X-ray scattering," *Adv. Mater.* **34**(6), 2107316 (2022).
17. W. Zhong et al., "Probing morphology and chemistry in complex soft materials with in situ resonant soft X-ray scattering," *J. Phys. Condens. Matter* **33**(31), 313001 (2021).
18. B.A. Collins and G. Eliot, "Resonant soft X-ray scattering in polymer science," *J. Polym. Sci.* **60** (7), 1199–1243 (2022).
19. G. Freychet et al., "Reconstructing the three-dimensional latent image of extreme ultraviolet resists with resonant soft X-ray scattering," *Proc. SPIE* **18**(2), 024003 (2019).
20. E. Gann et al., "Soft X-ray scattering facility at the Advanced Light Source with real-time data processing and analysis," *Rev. Sci. Instrum.* **83**, 045110 (2012)
21. H. Ikeura-Sekiguchi et al., "Characterization and degradation of ZEP520 resist film by TOF-PSID and NEXAFS," *J. Electron Spectrosc. Relat. Phenom.* **144**, 453–455 (2005).
22. G. K. Belmonte et al., "EUV photofragmentation and oxidation of a polyarylene–sulfonium resist: XPS and NEXAFS study," *J. Photochem. Photobiol. A: Chem.* **364**, 373–381 (2018).
23. R. Fallica et al., "Changes in the near edge X-ray absorption fine structure of hybrid organic–inorganic resists upon exposure," *Nanotechnology* **29**(36) 36LT03 (2018).
24. H. P. Yan et al., "Accurate and facile determination of the index of refraction of organic thin films near the carbon 1 s absorption edge," *Phys. Rev. Lett.* **110**(17), 177401 (2013).
25. B. L. Henke et al., "X-ray interactions: photoabsorption, scattering, transmission, and reflection at $E = 50–30,000$ eV, $Z = 1–92$," *At. Data Nucl. Data Tables* **54**(2), 181–342 (1993).
26. R. D. L. Kronig, "On the theory of dispersion of X-rays," *J. Optical Soc. Am.* **12**(6), 547–557 (1926).
27. E. Gann et al., "Quick AS NEXAFS Tool (QANT): a program for NEXAFS loading and analysis developed at the Australian synchrotron," *J. Synchrotron Radiat.* **23**(1), 374–380 (2016).
28. H. S. Suh et al., "Characterization of the shape and line-edge roughness of polymer gratings with grazing incidence small-angle X-ray scattering and atomic force microscopy," *J. Appl. Crystallogr.* **49**(3), 823–834 (2016).
29. V. Soltwisch et al. "Reconstructing detailed line profiles of lamellar gratings from GISAXS patterns with a Maxwell solver," *J. Appl. Crystallogr.* **50**(5), 1524–1532 (2017).
30. A. Andrle et al., "The anisotropy in the optical constants of quartz crystals for soft X-rays," *J. Appl. Crystallogr.* **54**, 402–408 (2021).
31. B. Shahriari et al., "Taking the human out of the loop: a review of Bayesian optimization," *Proc. IEEE* **104**, 148–175 (2016).
32. A. F. Herrero et al., "Analysis of line-edge roughness using EUV scatterometry," *Nanomanuf. Metrol.* **5**, 149–158 (2022).

33 A. F. Herrero et al., "Uncertainties in the reconstruction of nanostructures in EUV scatterometry and grazing incidence small-angle X-ray scattering," *Opt. Express* **29**, 35580–35591 (2021).

Qi Zhang received her PhD from Tsinghua University in 2019. Currently, she is a physicist research scientist at the Center for X-Ray Optics, Lawrence Berkeley National Laboratory (LBNL). Her research focuses on investigating resist fundamentals, particularly latent images, using resonant soft X-ray scattering techniques, as well as fabricating nanodevices based on two-dimensional materials using EUV lithography.

Kas Andrle completed their PhD at the Physikalisch-Technische Bundesanstalt (PTB) in Berlin, Germany. Currently, Kas Andrle serves at CHiPPS EFRC as a postdoc scholar at the LBNL. They integrate advanced tools, including a finite element method–based Maxwell solver and machine learning techniques, to push the boundaries of nanoscale analysis and innovation.

Cheng Wang received his PhD in physics from North Carolina State University in 2008. Currently, he is a physicist staff scientist at the Advanced Light Source, LBNL. He is a leading expert on the development of soft X-ray metrology and utilizes advanced synchrotron X-ray probes such as X-ray scattering, microscopy, and spectroscopy to elucidate the morphology, chemistry, and interfacial structure of a broad range of complex materials.

Biographies of the other authors are not available.